Article

# Fe-$TiO_2$ WITH LOW QUANTITY OF IRON EXTRACTED FROM (ILMENITE) MINING WASTE TO THE PHOTOCATALYTIC DEGRADATION OF CYANIDE IN WATER

**Yuli Marcela Henao-Hoyos[a,b,*], Marco Antonio Márquez-Godoy[b] and José G. Carriazo[a]**

[a]Departamento de Química, Facultad de Ciencias, Universidad Nacional de Colombia-Bogotá, carrera 30 No. 45-03, Ciudad Universitaria, 111321 Bogotá, Colombia

[b]Laboratorio de Biomineralogia y Biohidrometalurgia, Departamento de Materiales y Minerales, Facultad de Minas, Universidad Nacional de Colombia-Medellín, 050034 Medellín, Colombia

Received: 06/19/2023; accepted: 04/17/2024; published online: 06/25/2024

Nanoparticles of $TiO_2$ doped with low amount of Fe were synthesized from natural ilmenite obtained from alluvial gold mine wastes. The obtained $TiO_2$ were characterized using X-ray diffraction (XRD), X-ray fluorescence (XRF), Fourier-transform infrared spectroscopy (FTIR), UV-Vis diffuse reflectance, thermogravimetric analysis/differential scanning calorimetry (TGA/DSC), $N_2$ adsorption-desorption isotherms, transmission electron microscopy (TEM) and X-ray photoelectron spectroscopy (XPS). The results confirm the formation of mesoporous $TiO_2$ nanoparticles in anatase phase with 0.05 wt.% of iron possibly replacing some titanium places. All the characterizations were performed to the synthesized solid and the reference materials ($TiO_2$ anatase and Degussa P25). The photocatalytic activity of both the synthesized solid and references were evaluated in the photo-oxidation of cyanide in aqueous medium under UV illumination. An experimental design type Box-Behnken was performed choosing three different parameters: the initial concentration of cyanide (50, 150 and 250 ppm) the catalyst load (0.1, 0.5 and 1.0 g $L^{-1}$) and the oxygen source. The percentage of cyanide conversion was chosen as response in the design obtaining as optimal conditions $[CN^-]_0$ = 50 ppm, catalyst load = 0.6 g $L^{-1}$ and air bubbling. Under these conditions it was reached 32, 32 and 89% of cyanide conversion for Fe-$TiO_2$ synthesized, $TiO_2$ anatase and Degussa P25, respectively.

Keywords: heterogeneous photocatalysis; titanium dioxide; cyanide; photodecomposition; ilmenite.

## INTRODUCTION

Heterogeneous photocatalysis using titanium dioxide ($TiO_2$) is one of the most investigated photocatalytic process among the advanced oxidation process with the main purpose of pollutants elimination from water.[1] The photocatalytic activity of $TiO_2$ is originated from its electronic structure and photoelectric characteristics.[2] Titanium dioxide absorbs light in the UV region and generates reactive species (hydroxyl radicals •OH) that oxidize pollutants dissolved in water.[2] Although $TiO_2$ is chemically stable, non-toxic and has high reactivity, it is inactive under visible light due to its bandgap energy (3.2 eV).[3] To use solar light for the photoactivation of $TiO_2$, several authors[3] have investigated the doping of $TiO_2$ with different elements among which it can be found nonmetals like carbon, nitrogen and sulfur, and transition metals like Cu, Pt, Ag and Fe.

Several methods, such as sol-gel, hydrothermal, coprecipitation and impregnation have been implemented for the synthesis of $TiO_2$-based photocatalysts.[4-6] In the last decade, some authors[7-9] have investigated the synthesis of Fe-doped $TiO_2$ nanoparticles from ilmenite ores. The synthesis involves the leaching of both titanium and iron with sulfuric or hydrochloric acid in suitable concentrations, after which the synthesized solids have been used in photocatalytic reactions for degrading pollutants in water.

The reason for using ilmenite is that it represents the major source of titanium and titanium dioxide on Earth.[10] This mineral is commonly found in alluvial deposits associated with gold mining which are known as "black sands". After gold exploitation, these black sands become wastes that accumulates without any further benefit. Ilmenite ($FeTiO_3$) is present in black sands in high proportion, together with other minerals such as magnetite ($Fe_3O_4$), hematite ($Fe_2O_3$), monazite (Ce, La, Th($PO_4$)), zircon ($ZrSiO_4$), rutile ($TiO_2$), etc.[11,12]

Lee *et al.*[13] used natural ilmenite with moderate photocatalytic activity in the degradation of Reactive Black 5. The results of these authors encourage the investigation of the modification of ilmenite in order to obtain new synthetized solids with high photocatalytic activity. In the same way, Torres-Luna *et al.*[14] obtained Fe-doped $TiO_2$ after ilmenite leaching with sulfuric acid in different concentrations. They observed a red shift in the absorption of photons for all solids synthesized, as expected.

Organic dyes and pharmaceutical wastes are some of the most investigated pollutants to be decomposed by heterogeneous photocatalysis using $TiO_2$.[2,15] There are other pollutants rarely investigated, like inorganic compounds or toxic substances that require a basic pH to be manipulated and decomposed, such as the cyanide ions.[16] The cyanide ion consists of one atom of carbon connected to one atom of nitrogen by three molecular bonds ($C{\equiv}N^-$). Hydrogen cyanide is the molecular form that behaves as weak acid with p$K_a$ of 9.26. The major sources of cyanide in water are the wastewater coming from some metal mining process, electroplating manufacturing and metal cleaning industries.[17] Cyanide produces toxic effects at levels of 0.05 milligrams *per* deciliter of blood (mg $dL^{-1}$) or higher. Death have occurred at levels of 0.3 mg $dL^{-1}$ and higher (1 dL = 100 mL).[18] Treatments for removing cyanide include the chemical oxidation, natural attenuation and biodegradation, before being discharged to sewages. As an alternative procedure, the photodecomposition of cyanide using $TiO_2$ has also been proved with promising results.[16]

The aim of this work is to advance on designing effective $TiO_2$ nanostructures by using residual minerals (valorization of mineral wastes) with photocatalytic activity for elimination of toxic pollutants in water, i.e., the use of inorganic wastes for mitigation of pollution

*e-mail: ymhenaoh@unal.edu.co

Associate Editor handled this article: Marcela M. Oliveira

caused by other substances. In this work, the Fe-$TiO_2$ photocatalyst obtained by acid leaching of ilmenite concentrated from alluvial gold mines (Antioquia, Colombia) was used for the degradation of cyanide in water. The new synthesized material was compared with commercial references (anatase and $TiO_2$ Degussa P25).

## EXPERIMENTAL

### Materials

Ilmenite ($FeTiO_3$) was concentrated from black sands mineral residues yielded in mining processes of industrial alluvial gold exploitation in the Antioquia region (Colombia). The separation of ilmenite was carried out by both magnetic and electrostatic procedures using a Carpco magnetic separator Outokumpu and a Corona charging separator, respectively. Sulfuric acid (96%, Merck, Darmstadt, Germany), iron filings (small pieces of metallic iron) and sodium hydroxide (99%, Merck) were employed in the synthesis process. Degussa P25 ($TiO_2$) and $TiO_2$ anatase (Merck) were used as reference materials to compare the synthesized solid. All reagents used were analytical grade, and distilled or deionized water was used in the preparation of all solutions.

### Photocatalyst synthesis

Nanoparticulate Fe-$TiO_2$ was synthesized using the modified procedure of Torres-Luna *et al.*[14] The synthesis was performed by the simultaneous extraction of titanium and iron from the ilmenite previously concentrated by direct leaching with an aqueous solution of 50 wt.% of sulfuric acid. In a typical procedure, 50 g of this ilmenite was added to 250 mL of the sulfuric acid solution at 60 °C. The extraction was carried out in a conventional experimental setup which comprises a 500 mL three-neck round bottom flask provided with a reflux column and magnetic stirring. After a leaching period of 24 h, the excess of extracted iron was crystallized as ferrous sulfate. To concentrate the titanium/iron solution (a sol-gel system containing titanium oxysulfate) an evaporation process was necessary and iron filings were added to maintain the iron(II) in the solution. The crystallized ferrous sulfate was removed according the Equation 1.

$$FeTiO_{3(s)} + 2H_2SO_{4(aq)} \rightarrow TiOSO_{4(aq)} + FeSO_{4(s)} + 2H_2O_{(l)} \quad (1)$$

Before the final thermal hydrolysis, which will lead to the formation of titanium dioxide, the pH was increased to 1.4 using NaOH in small pellets. The temperature was increased to 96 °C, completing the reaction under refluxing for 6 h. Finally, the obtained solid was washed several times with distilled water (until the conductivity was near that of distilled water), dried at 100 °C for 24 h, and calcined for 2 h at 600 °C, milled and passed through a mesh ASTM 200.

### Characterization of solids

All the characterization was carried out for each one of the materials (synthesized Fe-$TiO_2$, $TiO_2$ anatase and $TiO_2$ Degussa P25). The determination of the chemical composition was made by X-ray fluorescence using an Epsilon 1 Malvern Analytics (Malvern, Worcestershire, UK) spectrophotometer. To study the structural properties of all solids, X-ray powder diffraction profiles were recorded using a Rigaku Miniflex equipment (Tokyo, Japan) with a copper radiation (Cu K$\alpha$, $\lambda$ = 1.54056Å). All diffractograms were made at room temperature in the 2$\theta$ range of 5 to 70°. Infrared spectra were taken from 400 to 4000 $cm^{-1}$ in a Shimadzu (Kyoto, Japan) spectrophotometer making compressed discs of the sample diluted in KBr (1 mg of sample in 100 mg of KBr). Textural characterization was performed by $N_2$ adsorption-desorption at 77 K. The samples were previously outgassed at 90 °C for 1 h and at 350 °C for 4 h. The Brunauer-Emmett-Teller (BET) surface areas ($S_{BET}$) were analyzed by nitrogen adsorption on an ASAP 2020 Micromeritics. Thermal analyses (TGA/DSC) were made with an SDT-Q600 TG/DTA (TA Instruments, New Castle, USA) instrument in a temperature range of 50-900 °C using a heating rate of 10 °C $min^{-1}$ under $N_2$ atmosphere. Transmission electron microscopy (TEM) images with energy-dispersive X-ray spectroscopy (EDS) were recorded using a FEI quanta Tecnai F20 Twin TMP (FEI company, Hillsboro, OR, USA) microscope. In order to determine the band-gap energies (Eg) the solids diffuse reflectance spectra (UV-Vis/DRS) were taken in the wavelength range of 200-900 nm using a Varian Cary 100 (Agilent Technologies, Santa Clara, CA, USA) spectrophotometer with integrating sphere. Furthermore, X-ray photoelectron spectroscopy (XPS) was used to analyze Ti-electron binding energies in the samples and obtain additional structural information. The analyses were performed in a X(NAP-XPS) Specs (Berlin, Germany) equipment with an analyzer PHOIBOS 150 1D-DLD using monochromatic $AlK_\alpha$ radiation (h$\nu$ = 1486.7 eV, 13 kV, 100 W) with a pass energy of 90 eV for survey spectra and 20 eV for the high-resolution spectra.

### Previous experimental design and optimization for the photocatalytic experiments

Several experimental parameters influence the reactions by heterogeneous photocatalysis within which are the photoreactor geometry, irradiation source, photocatalyst disposal (suspension or immobilized) temperature, time of irradiation, pH, oxygen supplier, photocatalyst amount, model compounds for photocatalyst tests, initial concentration of model compound.[19] Any of those parameters could be considered as an independent variable. In this work we maintained constant the photoreactor geometry, irradiation source, photocatalyst disposal (suspension) temperature, pH, irradiation time and the model compound that corresponds to cyanide.

Regarding the independent variables, three parameters were chosen to be studied: the amount of catalyst, initial concentration of cyanide and the oxygen supplier. This latter enhances the conversion of cyanide because it acts as an acceptor of photogenerated electrons.[2] A response surface methodology (RSM) was implemented with the purpose of obtaining the best experimental conditions alongside the lower number of experiments. The Box-Behnken design (BBD) was used in this work which comprises three factors that corresponds to independent variables with three levels for each one, as can be seen in Table 1. The response measured corresponds to the cyanide conversion percentage. From these factors and levels, the design suggests to perform 15 experiments to make the optimization (see Supplementary Material, Table 1S).

**Table 1.** Experimental range and levels values for independent variables

| Factor | Low level | Middle level | High level |
|---|---|---|---|
| $[CN^-]_0$ / ppm | 50 | 150 | 250 |
| Oxygen supplier | - | $H_2O_2$ (20 µL 30%) | air bubbling |
| Catalyst load / (g $L^{-1}$) | 0.1 | 0.5 | 1.0 |

Furthermore, in order to compare the photocatalytic performance of the Fe-$TiO_2$ synthetized with respect to commercial references (anatase and Degussa P25) after the optimization, a set of experiments were performed under the same conditions.

### Photocatalytic experiments

A semi-batch cylindrical reactor of glass opened to the atmosphere provided with a jacket loop containing water connected to a thermostat at 20 °C was used for all photocatalytic reactions. All experiments were performed with a solution volume of 400 mL under constant UV irradiation with a 13 W low-pressure UV mercury lamp for 4 h and magnetic stirring (500 rpm). The external surface of the reactor was covered with aluminum foil to prevent the influence of sunlight. The light intensity of the lamp was measured using Parker's actinometer ($9.04 \times 10^{12}$ counts $cm^{-3}$ $s^{-1}$ which corresponds to 0.008 mW $cm^{-2}$).[20] Before starting the reaction, the system was maintained under constant stirring for 1 h in absence of light to reach the adsorption-desorption equilibrium. NaOH and moisture filters were installed in the air line previous to the reactor with the purpose to retain the $CO_2$ and water contained in air. The air was bubbled into the solution with the UV lamp on. Aliquots of constant volume (3 mL) were taken at regular intervals of time and filtered (Millipore 0.45 μm) for cyanide quantification by $CN^-$ ion selective electrode (HI 4109 Hanna Instruments) and volumetric quantification with standard $AgNO_3$ using the APHA method 4500-D.[21] As mentioned above, the experimental parameters considered in this work were the initial concentration of cyanide, the load of catalyst and the oxygen supplier.

## RESULTS AND DISCUSSION

### Characterization

*X-Ray fluorescence spectroscopy (XRF)*

The ilmenite obtained from black sands wastes from gold mining showed an important content of titanium (26.13% = $3.27 \times 10^{-3}$ mol Ti $g^{-1}$ of ilmenite) and iron (55.90% = $7.00 \times 10^{-3}$ mol Fe $g^{-1}$ of ilmenite) with minor quantities of zirconium (1.28%), manganese (1.23%), silicon (2.11%), aluminum (0.901%), and vanadium (0.512%) impurities. Table 2 shows the iron and titanium contents for the photocatalyst synthesized from ilmenite and for the references (commercial anatase and Degussa P25). As it can be seen, the resulting solid has a similar content of iron and titanium comparable to the commercial $TiO_2$ Degussa P25. This indicates that the experimental conditions allowed a high extraction of titanium from the ilmenite concentrated from the mining waste. The quantity of iron incorporated in the synthesized Fe-$TiO_2$ was appreciably low because of the efficient separation of ferrous sulfate crystallization step.[22,23]

*X-Ray diffraction (XRD)*

All patterns presented in Figure 1 were compared with the diffraction lines of JCPDS for each mineral and for $TiO_2$. Figure 1a shows the XRD pattern obtained for the concentrated ilmenite. As expected, this concentrate remains with impurities of other minerals as zircon, hematite and rutile present in the original mining waste of black sands. However, there are characteristic peaks with high intensity corresponding to ilmenite (2θ = 23.94, 32.45, 32.85, 35.55, 53.62, and 63.78°) supporting the presence of ilmenite as component of this powder.[14]

Figure 1b presents the XRD patterns for the evaluated photocatalysts. From the XRD pattern of the photocatalyst obtained in the present work (Fe-$TiO_2$) it can be seen that all the peaks correspond to the crystalline phase anatase.[2] It is an interesting result knowing that the anatase phase is more photoactive than the rutile phase.[2] Furthermore, it can be observed a comparison between XRD profiles that include anatase and Degussa P25. The latter contains both anatase and rutile phases which confirms that the only crystalline phase obtained for the $TiO_2$ synthesized in the present work corresponds to anatase. In the Figure 1b the highest intensity peak (2θ = 25.2°) corresponding to the crystallographic plane (110) was used to calculate these average particles sizes using the Scherrer equation.[24] The average crystallites sizes obtained are 54.4, 156.8 and 69.7 nm for the synthesized photocatalyst, anatase and Degussa P25, respectively. It is worth noting that crystallite determinations are underestimated because instrumental broadening has not been considered. The crystallite size for the synthesized Fe-$TiO_2$ is lower than those reference solids which could be related to the thermal, acid and kinetic conditions of the hydrolysis for the formation of titanium dioxide. It is noteworthy that a possible isomorphic substitution of iron(III) in the anatase structure is difficult to be verified in the XRD pattern because the ionic radius of Fe (0.64 Å) is very similar to that of Ti (0.68 Å).[14]

**Table 2.** Chemical composition (quantities expressed as moles were calculated)

| Photocatalyst | Fe / % | Ti / % | S / % | Fe / mol | Ti / mol | Molar / %Fe[a] |
|---|---|---|---|---|---|---|
| FT_1_600 (Fe-$TiO_2$) | 0.050 | 53.15 | 0.46 | $8.95 \times 10^{-4}$ | 1.11 | 0.081 |
| Degussa P25 | 0.013 | 53.61 | 0.02 | $2.33 \times 10^{-4}$ | 1.12 | 0.021 |
| Anatase | 0.014 | 50.89 | 0.03 | $2.51 \times 10^{-4}$ | 1.06 | 0.022 |

[a]Molar percentage was calculated as [(mol Fe)/(mol Fe + mol Ti)] × 100.

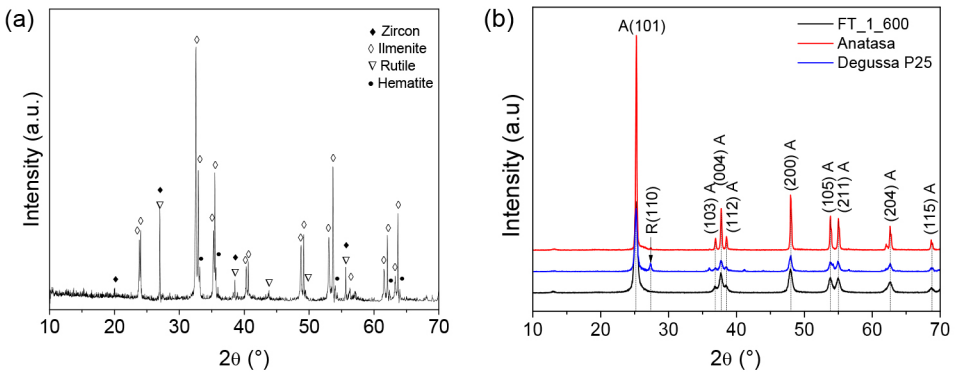


***Figure 1.*** *XRD patterns for (a) ilmenite and (b) synthesized Fe-$TiO_2$ (FT_1_600), reference anatase and commercial Degussa P25. A: anatase; R: rutile*

*UV-Vis diffuse reflectance spectroscopy*

Diffuse reflectance UV-Vis spectra for the Fe-$TiO_2$ and commercial references are showed in Figure 2a. Kubelka-Munk function ($F(R_\infty) = (1 - R^2)/2R$) was used to determine the band gap of the solids from the reflectance data.[25] As can be seen in Figure 2a, Fe-$TiO_2$, the reference anatase and Degussa P25 exhibit their maximum of absorbance about 354 nm. However, it is important to highlight that reference anatase and commercial Degussa 25 do not absorb radiation above 400 nm. Meanwhile synthesized Fe-$TiO_2$ showed an important absorbance in this wavelength and even above. This result indicates a shift toward wavelengths in the visible region which is correlated with a decrease in the band gap energy. Therefore, although the content of iron in the synthesized Fe-$TiO_2$ is just of 0.05 wt.%, it could be considered that this solid is doped with iron.[23,26] Solano Pizarro and Herrera Barros,[26] argue that the extended absorption to the visible region is attributed to the electron transition from Fe3d orbitals to the $TiO_2$ conduction band.

To determine the band-to-band transitions of the solids, the absorption data was adjusted for indirect band gap transition using the Tauc Plots $((F(R) \times h\nu)^n$ *vs.* $h\nu)$.[25] Here, F(R) corresponds to Kubelka-Munk function, $h\nu$ is the energy in eV and n indicate the transition, n = 1/2 when the electronic transition is indirect and n = 2 when it is direct. In the case of titanium dioxide, it is known that the electronic transition is indirect, therefore the value set for n is n = 1/2. The band gap values were obtained from the extrapolation of indirect transitions plots showed in the Figure 2b. The value of band gap energy for synthesized Fe-$TiO_2$ (3.06 eV) is very similar to that one of $TiO_2$ Degussa P25 (3.00 eV) and lower than to that of commercial anatase (3.15 eV). As it was pointed above this result can obey to the presence of iron within the $TiO_2$ structure in the Fe-$TiO_2$.[7] The presence of iron doping can cause structural defects in the crystal lattice introducing impurities or defects inducing local states below the conduction band edge.[26,27]

*Fourier-transform infrared spectroscopy (FTIR)*

IR spectrum of ilmenite is shown in the Figure 3a. The spectrum presents characteristic bands for ilmenite at 632, 543 and 461 $cm^{-1}$ associated to vibrations of metal-oxygen bonds.[28] The bands about 3431 and 1626 $cm^{-1}$ correspond to stretching and blending vibrations of the O–H bonds probably as consequence from the adsorbed water.[14]

IR spectrum for the synthesized Fe-$TiO_2$ showed all the typical signals that both the reference anatase and commercial Degussa P25 exhibit, Figure 3b. Two weak bands appear about 1134 and 1042 $cm^{-1}$ for Fe-$TiO_2$ which correspond to the sulfate group. It was expected because the methodology used for the synthesis could allow residual sulfate groups after washing the synthesized Fe-$TiO_2$.[14] Remaining sulfur was also detected by chemical composition analysis (Table 2). Bands observed at 3400 and 1626 $cm^{-1}$ correspond to stretching and blending vibrations of O–H bonds of the adsorbed water.[26] About 445 and 675 $cm^{-1}$ two strong bands overlap which correspond to stretching and blending vibrations of metal-oxygen bonds that in this case are Fe–O, Ti–O.[14,23,26]

*BET surface analysis*

$N_2$ adsorption-desorption isotherms were performed for the synthesized Fe-$TiO_2$ (FT_1_600), the reference anatase and $TiO_2$ Degussa P25. Fe-$TiO_2$ synthesized in the present work exhibits a combination of an isotherm type II and IVa because the nanoparticle size indicating that despite it could be classified a macroporous solid it has a pore size closer to mesoporous range.[29] The hysteresis loops of this solid have tendency to H1 which is characteristic of pores with uniform shape and size, i.e., a narrow range of uniform mesopores.[29] In the case of the references anatase and Degussa P25 the isotherms are type II which is characteristic of macroporous or nonporous solids. The hysteresis for those solids corresponds to H3 (Figure S1, Supplementary Material).

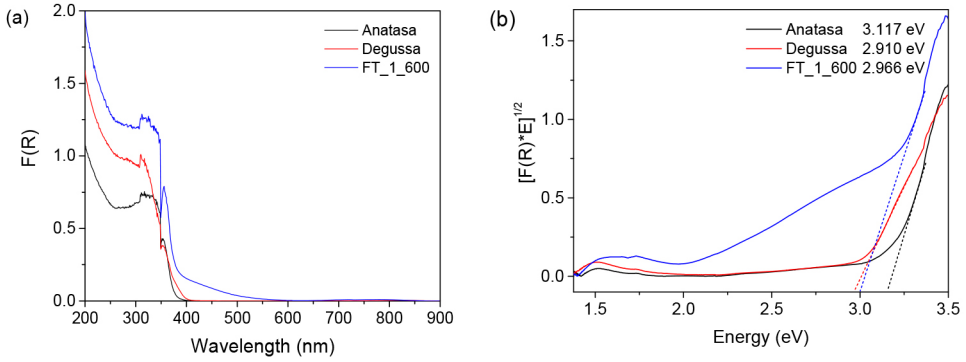


***Figure 2.*** *(a) UV-Vis diffuse reflectance spectra and (b) Tauc plots for indirect transition and band gap energies for synthesized Fe-$TiO_2$ (FT_1_600), commercial anatase and $TiO_2$ Degussa P25*

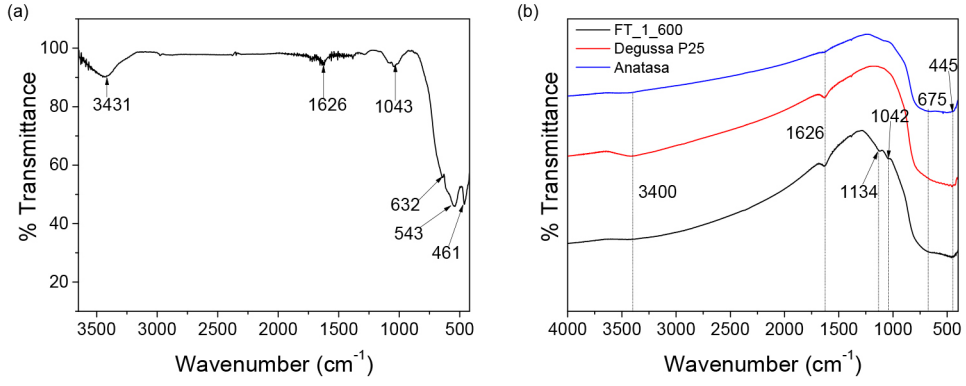


***Figure 3.*** *Infrared spectra for the (a) ilmenite concentrated from mining waste and (b) synthesized Fe-$TiO_2$ (FT_1_600) and the commercial reference (anatase and $TiO_2$ Degussa P25)*

The surface area for the photocatalyst Fe-$TiO_2$ (71 $m^2$ $g^{-1}$) is higher than those of the reference anatase (12 $m^2$ $g^{-1}$) and the $TiO_2$ Degussa P25 (48 $m^2$ $g^{-1}$). The surface area of synthesized Fe-$TiO_2$ is favorable to the adsorption and photocatalytic process for a target substrate.[30] Similar (or lower) values of surface areas have been reported by other authors[23,31] nano-sized synthetic rutile and anatase obtained from ilmenite or other precursors. In general, high surface area and a small particle size are favorable to the adsorption and photocatalytic process.[19]

*X-Ray photoelectronic spectroscopy (XPS)*

Figure 4a shows the XPS survey spectrum for the Fe-$TiO_2$ synthesized in the present work, reference anatase and commercial $TiO_2$ Degussa P25. All the solids present the same signals for Ti, O and C elements with sharp photoelectron peaks appearing at binding energies of 459.6 eV (Ti 2p) 530.3 eV (O 1s) and 288.6 eV (C 1s). The carbon peak is attributed to adventitious hydrocarbon from XPS instrument itself.[32] Although the confirmation of iron presence was made by chemical analysis, for the synthesized Fe-$TiO_2$ it could not be observed neither by the survey spectrum nor through the high-resolution spectra. The same result was also noted by Sohrabi and Akhlaghian,[33] after obtaining Fe/$TiO_2$ by sol-gel method that was tested in the phenol photodegradation. In this case the authors obtained an iron doping level of 0.20 wt.% in the synthesized solid. XPS detection limit is estimated to be in the range 1 to 0.1 at.% whose exact sensibility may be directly dependent on the equipment.[34] From the chemical composition results it is possible to calculate the atomic percentage for the iron in the Fe-$TiO_2$ synthesized in our work which corresponds to 0.08 at.% Fe. Such value confirms that this quantity of iron cannot be analyzed by XPS and would be necessary to be analyzed by X-ray absorption spectroscopy (XAS) as explained by Parrino *et al*.[19] It is worth noting that due to the similarity between ionic radius of $Fe^{3+}$ (0.64 Å) and $Ti^{4+}$ (0.68 Å) the substitution $Fe^{3+}$ by $Ti^{4+}$ in the $TiO_2$ structure can occur which increases the number of electrons in the $TiO_2$ conduction band favoring the generation of $Ti^{3+}$ on the surface.[33]

High resolution spectra of Ti and O for $TiO_2$ synthesized here and for the reference materials are compared in the Figures 4b and 4c. As observed in Figure 4b, the binding energy values for Ti $2p_{1/2}$ and Ti $2p_{3/2}$ of synthesized Fe-$TiO_2$ are between those for reference anatase and $TiO_2$ Degussa P25. The binding energy values of synthesized Fe-$TiO_2$ are shifted towards lower energy sites than those of commercial anatase but shifted towards higher energy position than $TiO_2$ Degussa P25. It means that the titanium has a slightly different electronic environment in the synthesized Fe-$TiO_2$ in comparison with the $TiO_2$ taken as reference. It could be explained by the possible substitution of $Fe^{3+}$ by $Ti^{4+}$ in the $TiO_2$ structure.[7] The incorporation of $Fe^{3+}$ ions in the place of $Ti^{4+}$ possibly increase the $Ti^{3+}$ character (*vide supra*) facilitating the electron extraction and a shifting the peaks towards lower binding energy values. For this reason, it can be considered that some iron ions were incorporated in the $TiO_2$ lattice of the photocatalyst synthesized in the present work with the resulting displacement of the XPS Ti2p signals.[32,35] Figure 4c shows the O1s binding energy values and shifts for all the solids. O1s peak appears at 534.4 eV for the synthesized Fe-$TiO_2$ (FT_1_600), at 532.2 eV for commercial anatase and 528.9 eV for $TiO_2$ Degussa P25.[36]

The higher energy position (and broad signal) of O1s at 534.4 eV for the synthesized Fe-$TiO_2$ is attributed to the interaction of $TiO_2$ oxygen with sulfate groups.[37,38] As it has been mentioned above iron was not detected by this XPS analysis and therefore in the range of binding energies from 695 to 730 eV there was no signal (Figure 4d). No explanation is known for the differences found between the XPS positions of commercial anatase and $TiO_2$ Degussa P25 since we do not have information on the synthesis of those samples.[39,40]

*Transmission electron microscopy (TEM)*

TEM images of different studied materials were took and are presented in Figure 2S, Supplementary Material. All solids presented nanoparticles with nearly spherical shape. The particles in the synthesized Fe-$TiO_2$ are agglomerated. It agrees with the results obtained by $N_2$ adsorption-desorption isotherms (hysteresis H1 for agglomerates of spheroidal particles). The single particle sizes of the

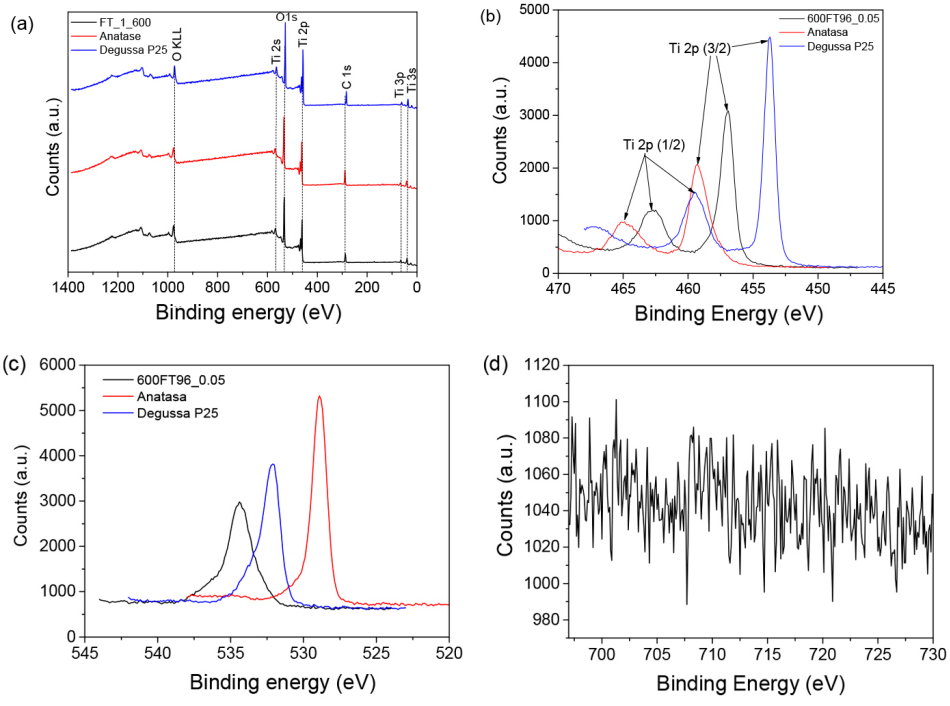


***Figure 4.*** *XPS analyses for synthesized Fe-$TiO_2$ (FT_1_600), commercial anatase and $TiO_2$ Degussa. (a) Comparison of the survey spectra, (b) high resolution spectra of Ti2p, (c) high resolution spectra of O1s and (d) XPS position of high resolution spectra for $Fe^{III}$ in the Fe-$TiO_2$ (FT_1_600)*

nanoparticles were between 6 and 27 nm. The particles for synthesized Fe-$TiO_2$ and $TiO_2$ Degussa P25 are nearly equal in size (Figure 2S). Meanwhile the particles from the commercial anatase are much bigger than those for Fe-$TiO_2$ and Degussa P25 (Figure S2). The particle sizes for $TiO_2$ Degussa P25 were between 11 and 42 nm and between 51 and 235 nm for the commercial anatase. These results agree with the average crystallite sizes obtained through XRD studies using the Scherrer equation.

*Thermal analysis*

Thermogravimetric analysis (TGA) and differential scanning calorimetry (DSC) were performed with the purpose of observing the thermic stability of the Fe-$TiO_2$ synthesized photocatalyst. TGA-DSC curves were obtained for the synthesized Fe-$TiO_2$, $TiO_2$ Degussa P25 and commercial anatase (Figure 3S, Supplementary Material). The TGA profile of Fe-$TiO_2$ reveals three weight losses (Figure 3Sa) where the first one at 82.45 °C is attributed to physically adsorbed water because it is a temperature lower than 120 °C; the second loss at 259.5 °C can be assigned to elimination of surface OH groups and the last loss at 683.3 °C corresponds to the elimination of both structural OH groups and residuals sulfate groups remaining from the synthesis process.[19] The presence of sulfate groups had already been confirmed by the infrared spectroscopy and XRF results. In the case of the reference anatase and Degussa P25 (Figures 3Sb and 3Sc) is just observed one loss of weight in a range of temperature between 50 and 500 °C which corresponds to the elimination of adsorbed water and structural O–H groups (dehydroxylation). Regarding DSC curves, a high similarity was detected for the profiles of Fe-$TiO_2$ and the reference materials showing a continuous endothermic trend and a drop above 800 °C, perhaps as consequence of continuous dehydroxylations and the final transformation of anatase to rutile, respectively. Finally, the thermal stability of the synthesized Fe-$TiO_2$ is good and similar to that of reference materials.

*Experimental results for optimization of catalytic experiments*

See Supplementary Material.

*Photocatalytic activity*

The photocatalytic degradation for cyanide was performed using the synthesized Fe-$TiO_2$, the reference anatase and $TiO_2$ Degussa P25. The catalyst tests were performed under optimized conditions suggested by the BBD. Figure 5 shows the % conversion of cyanide as a function of time under UV light irradiation. The synthesized Fe-$TiO_2$ reached 31.5% of cyanide conversion after 4 h of reaction while the commercial anatase and $TiO_2$ Degussa P25 reached 31.9 and 87.9%, respectively. Although the conversion of cyanide is higher using Degussa P25, it is an important advance regarding the synthesis of $TiO_2$ photocatalysts from ilmenite powders recovered from mining wastes.

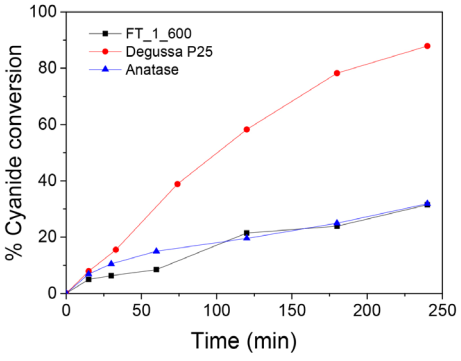


***Figure 5.*** *Photocatalytic degradation of cyanide (% cyanide conversion as a function of UV-light irradiation time) by Fe-$TiO_2$ synthesized in the present work and the reference materials (commercial anatase and $TiO_2$ Degussa P25). Experimental conditions: catalyst load = 0.6 g $L^{-1}$, $[CN^-]_0$ = 50 ppm, pH = 10, Temperature = 20 °C*

*Mechanistic aspects*

The primary process after UV radiation absorption by the photocatalyst is the electron/hole pairs ($e^-/h^+$) photogeneration, as it is shown in the Equation 2.[2] The cyanide photo-oxidation by $TiO_2$ may occur through direct charge transfer with the photogenerated holes ($h^+$) (Equation 3) or an indirect pathway with the adsorbed or diffused hydroxyl radicals (•OH) by the aqueous medium (Equation 4). If the reaction is accompanied by $O_2$, the oxygen might act as an electron scavenger and reacts with the photogenerated electrons (Equation 5).[41] It is accepted that the photodegradation mechanism of cyanide implies the oxidation of $CN^-$ to $CNO^-$, through either photogenerated holes (Equation 3) or hydroxyl radicals (•OH) (Equation 6).[42,43]

$$TiO_2 + h\nu \rightarrow TiO_2 + e^-_{CB} + h^+_{VB} \quad (2)$$

$$CN^- + 2HO^- + 2h^+ \rightarrow CNO^- + H_2O \quad (3)$$

$$TiO_2 - OH^-_s + h^+ \rightarrow TiO_2 - OH^{\bullet}_{ads} \quad (4)$$

$$O_2 + 2e^- + 2H_2O \rightarrow H_2O_2 + 2HO^- \quad (5)$$

$$2TiO_2 - OH^{\bullet}_{ads} + CN^- \rightarrow 2TiO_2 + CNO^- + H_2O \quad (6)$$

$$CNO^- + 3H_2O + 6h^+ \rightarrow NO_2^- + CO_2 + 6H^+ \quad (7)$$

$$NO_2^- + H_2O + 2h^+ \rightarrow NO_3^- + 2H^+ \quad (8)$$

$$CNO^- + 2H_2O + 3h^+ \rightarrow CO_3^{2-} + 1/2N_2 + 4H^+ \quad (9)$$

$$2CNO^- + 8OH^- + 6h^+ \rightarrow 2CO_3^{2-} + N_2 + 4H_2O \quad (10)$$

$$CNO^- + H_2O + OH^- \rightarrow CO_3^{2-} + NH_3 \quad (11)$$

Depending on the oxidizing conditions, cyanate can undergo further oxidation to different subproducts.[42,44] Auguglario *et al.*[42] say that the addition of oxygen or air to the reaction medium determine the mild oxidation conditions, and as consequence the formation of volatile nitrogen-containing species (such as $NH_3$, $N_2$, $N_2O$, etc.) is promoted together with generation of nitrite ($NO_2^-$) and nitrate ($NO_3^-$) ions. Under strong oxidizing conditions, such as those with large amounts of $H_2O_2$, volatile nitrogen-containing species are not produced, or they are quickly photo-oxydized to $NO_2^-$ and $NO_3^-$ as it was observed in the Equations 7 and 8. All the possible reactions of cyanate oxidation were described in Equations 7-11. In this work, air was employed as $O_2$ source and the photocatalytic oxidation occurs in aqueous medium. Therefore, it is expected the oxidation of cyanide to cyanate, and even a further oxidation to volatile species such as it was mentioned above. The possible mechanism of photo-oxidation of cyanide under current conditions could be represented by Equations 2-11 described above, except for the Equations 7 and 8, which can occur only under strong oxidizing conditions.

## CONCLUSIONS

This work demonstrates the viability for obtaining an Fe-doped $TiO_2$ photocatalyst by acid treatment of natural ilmenite powders from alluvium gold mining wastes. The characterization by XRD allows determining the crystalline phase of the synthesized solid,

which corresponds to anatase structure. All the characterizations performed on the sample suggested that the synthesized Fe-$TiO_2$ was doped with a small quantity of iron. This result was verified by XRF, XRD and XPS. Regarding the experimental design (Box-Behnken Design), it is worth mentioning that although the optimized model is not enough adjusted ($R^2 = 0.81$) for the selected factors and levels, the studied parameters were well correlated. The photocatalytic reactions, under optimized conditions, showed important conversions of cyanide for Fe-$TiO_2$, $TiO_2$ anatase and Degussa P25 (32, 32 and 88%, respectively). These results suggest that the catalyst Fe-$TiO_2$ obtained from the natural ilmenite exhibits a similar photoactivity to that of $TiO_2$ (anatase) used as reference. Although $TiO_2$ Degussa P25 is more active under UV irradiation, the obtained results with Fe-$TiO_2$ are promising because this catalyst was synthesized from mining wastes. Finally, according to the band-gap of the solid Fe-$TiO_2$, this material can be evaluated under visible irradiation, with potentially better results in the reaction of cyanide in diluted aqueous medium.

## ACKNOWLEDGMENTS

We thank to Ministry of Sciences of Colombia who supported this work through the grant 785 for National Doctorates of 2017 and to Mineros SA for donating the samples. This work was developed in the Laboratory of Catalysis and Nanomaterials and the Laboratory of Applied Biomineralogy from the National University of Colombia.

The authors declare that they have no conflict of interest.

## SUPPLEMENTARY MATERIAL

Complementary material for this work is available at http://quimicanova.sbq.org.br/, as a PDF file, with free access.

## REFERENCES

1. Boczkaj, G.; Fernandes, A.; *Chem. Eng. J.* **2017**, *320*, 608. [Crossref]
2. Yao, X.; Jin, H.; Liu, C.; Chuang, S. S. C.; *$TiO_2$-Based Photocatalytic Conversion Processes: Insights from In Situ Infrared Spectroscopy*, Elsevier: Amsterdam, 2020
3. Schneider, J.; Matsuoka, M.; Takeuchi, M.; Zhang, J.; Horiuchi, Y.; Anpo, M.; Bahnemann, D. W.; *Chem. Rev.* **2014**, *114*, 9919. [Crossref]
4. Jami, M.; Dillert, R.; Suo, Y.; Bahnemann, D. W.; Wark, M.; *Int. J. Photoenergy* **2018**, *2018*, 1. [Crossref]
5. Lan, K.; Wang, R.; Zhang, W.; Zhao, Z.; Elzatahry, A.; Zhang, X.; Liu, Y.; Al-Dhayan, D.; Xia, Y.; Zhao, D.; *Chem* **2018**, *4*, 2436. [Crossref]
6. Martins, A. C.; Cazetta, A. L.; Pezoti, O.; Souza, J. R. B.; Zhang, T.; Pilau, E. J.; Asefa, T.; Almeida, V. C.; *Ceram. Int.* **2017**, *43*, 4411. [Crossref]
7. Thambiliyagodage, C.; Wijesekera, R.; Bakker, M. G.; *Discovery Materials* **2021**, *1*, 20. [Crossref]
8. Lee, R. B.; Lee, K. M.; Lai, C. W.; Pan, G. T.; Yang, T. C. K.; Juan, J. C.; *Adv. Powder Technol.* **2018**, *29*, 1779. [Crossref]
9. Shao, S.; Yu, J.; Love, J. B.; Fan, X.; *J. Alloys Compd.* **2021**, *858*, 158388. [Crossref]
10. Nguyen, T. H.; Lee, M. S.; *Miner. Process. Extr. Metall. Rev.* **2019**, *40*, 231. [Crossref]
11. Lamus Molina, C. M.: *Mineralogía Aplicada al uso y Aprovechamiento de las Arenas Negras (El Bagre, Antioquia)*; Maestría en Ingeniería de Materiales y Procesos, Universidad Nacional de Colombia, Medellín, 2005. [Link] accessed in June 2024
12. Bendeck, J. L. K.: *Caracterización y Aprovechamiento de Recursos Minerales en Colas de Terrazas Aluviales del Distrito Bagre-Nechí*; Maestría en Recursos Minerales, Universidad Nacional de Colombia, Medellín, 2016. [Link] accessed in June 2024
13. Lee, R. B.; Juan, J. C.; Lai, C. W.; Lee, K. M.; *Chin. Chem. Lett.* **2017**, *28*, 1613. [Crossref]
14. Torres-Luna, J. A.; Sanabria, N. R.; Carriazo, J. G.; *Powder Technol.* **2016**, *302*, 254. [Crossref]
15. Kozlova, E. A.; Valeeva, A. A.; Sushnikova, A. A.; Zhurenok, A. V.; Rempel, A. A.; *Nanosyst.: Phys., Chem., Math.* **2022**, *13*, 632. [Crossref]
16. Wei, P.; Zhang, Y.; Huang, Y.; Chen, L.; *J. Mol. Liq.* **2023**, *377*, 121519. [Crossref]
17. United States Environmental Protection Agency (US EPA); *Cyanide Compounds, 74-90-8*, EPA's Integrated Risk Information System (IRIS), 2016. [Link] accessed in June 2024
18. Agency for Toxic Substances and Disease Registry, https://www.atsdr.cdc.gov/toxprofiles/tp8-c1.pdf, accessed in June 2024.
19. Parrino, F.; Loddo, V.; Augugliaro, V.; Camera-Roda, G.; Palmisano, G.; Palmisano, L.; Yurdakal, S.; *Catal. Rev.: Sci. Eng.* **2019**, *61*, 163. [Crossref]
20. Hatchard, C. G.; Parker, C. A.; *Proc. R. Soc. London, Ser. A* **1956**, *235*, 518. [Crossref]
21. American Public Health Association (APHA); *Standard Methods for the Examination of Water and Wastewater*, 20th ed.; American Public Health Association: Washington, 1999.
22. Chernet, T.; *Mineral. Petrol.* **1999**, *67*, 21. [Crossref]
23. Khan, M. S.; Shah, J. A.; Riaz, N.; Butt, T. A.; Khan, A. J.; Khalifa, W.; Gasmi, H. H.; Latifee, E. R.; Arshad, M.; Al-Naghi, A. A. A.; Ul-Hamid, A.; Arshad, M.; Bilal, M.; *Nanomaterials* **2021**, *11*, 1. [Crossref]
24. Azaroff, L. V.; Buerger, M. J.; *The Powder Method in Crystallography*, 1st ed.; McGraw-Hill: New York, 1958.
25. López, R.; Gómez, R.; *J. Sol-Gel Sci. Technol.* **2012**, *61*, 1. [Crossref]
26. Solano Pizarro, R. A.; Herrera Barros, A. P.; *Advanced Composites Letters* **2020**, *28*, 1. [Crossref]
27. Castillo, J.; Rodriguez, F.; López-Malo, A.; Sanchez-Mora, E.; Quiroz, M.; Bandala, E.; *J. Technol. Innovations Renewable Energy* **2015**, *4*, 1. [Crossref]
28. Chukanov, N. V.; *Infrared Spectra of Mineral Species*, 2014th ed.; Springer-Verlag: Dordrecht, 2014.
29. Thommes, M.; Kaneko, K.; Neimark, A. V.; Olivier, J. P.; Rodriguez-Reinoso, F.; Rouquerol, J.; Sing, K. S. W.; *Pure Appl. Chem.* **2015**, *87*, 1051. [Crossref]
30. Byrne, C.; Subramanian, G.; Pillai, S. C.; *J. Environ. Chem. Eng.* **2018**, *6*, 3531. [Crossref]
31. Tran, C. V.; Nguyen, P. T. H.; Nguyen, D. A.; Le, B. T.; Truong, T. N.; La, D. D.; *International Journal of Advanced Engineering, Management and Science* **2018**, *4*, 574. [Crossref]
32. Goswami, P.; Ganguli, J. N.; *Mater. Res. Bull.* **2012**, *47*, 2077. [Crossref]
33. Sohrabi, S.; Akhlaghian, F.; *J. Nanostruct. Chem.* **2016**, *6*, 93. [Crossref]
34. Shard, A. G.; *Surf. Interface Anal.* **2014**, *46*, 175. [Crossref]
35. Meng, H.; Wang, B.; Liu, S.; Jiang, R.; Long, H.; *Ceram. Int.* **2013**, *39*, 5785. [Crossref]
36. Mahajan, J.; Jeevanandam, P.; *New J. Chem.* **2018**, *42*, 2616. [Crossref]
37. Kim, M. R.; Woo, S. I.; *Appl. Catal., A* **2006**, *299*, 52. [Crossref]
38. Jung, S. M.; Dupont, O.; Grange, P.; *Appl. Catal., A* **2001**, *208*, 393. [Crossref]
39. Reddam, H. A.; Elmail, R.; Lloria, S. C.; Monrós Tomás, G.; Reddam, Z. A.; Coloma-Pascual, F.; *Bol. Soc. Esp. Ceram. Vidrio* **2020**, *59*, 138. [Crossref]
40. Bagus, P. S.; Ilton, E. S.; Nelin, C. J.; *Surf. Sci. Rep.* **2013**, *68*, 273. [Crossref]
41. Pelizzetti, E.; Serpone, N.; *Homogeneous and and Heterogeneous Photocatalysis*, 1st ed.; Springer: Dordrecht, 1986.
42. Augugliaro, V.; Loddo, V.; Marcì, G.; Palmisano, L.; López-Muñoz, M. J.; *J. Catal.* **1997**, *166*, 272. [Crossref]
43. Koohestani, H.; *Micro Nano Lett.* **2019**, *14*, 45. [Crossref]
44. Frank, S. N.; Bard, A. J.; *J. Phys. Chem.* **1977**, *81*, 1484. [Crossref]